LAWRENCE
LIVERMORE
NATIONAL
LABORATORY

LLNL-JRNL-556451

A Simple Interphase Coupling Model for Shock Interaction with a Deformable Particle

Y. Ling, A. Haselbacher, S. Balachandar, F. Najjar, D. Stewart

May 8, 2012

Journal of Applied Physics

Disclaimer

Noname manuscript No.
(will be inserted by the editor)

A Simple Interphase Coupling Model for Shock Interaction with a Deformable Particle

Y. Ling · A. Haselbacher · S. Balachandar · F. M. Najjar · D. S. Stewart

Received: XXX TO BE DONE XXX / Accepted: XXX TO BE DONE XXX

Abstract The interaction between an intense shock and deformable particles is an important phenomena in several technical applications. Typical applications involve a large number of particles and the length scales of interest are much larger than the particle size. Therefore, it is impractical to resolve the details of shock-particle interaction on the particle scale and the coupling between particles and ambient medium is represented by the particle force and heating models. For example, in the process of multiphase explosive detonation, the density of the detonation products is substantial and thus significant momentum and energy transfer occurs during the initial shock-particle or detonation-particle interaction. Since the post-detonation pressure in condensed explosives can be significantly larger than the yield strength of materials, the particles can experience significant deformation and compression heating, which makes modeling of interphase coupling challenging. In this paper, scaling analysis and direct numerical simulations (DNS) are conducted to investigate the interaction between an intense shock and a deformable particle. A simple physics-based interphase coupling model is proposed that takes into account the essential effects of particle deformation and unsteady mechanisms on momentum and energy transfer. The model prediction is compared against DNS results, and reasonable agreement is observed.

Keywords Shock wave · Multiphase flows · Interphase coupling · Condensed matter

Y. Ling
Department of Mechanical and Aerospace Engineering
University of Florida
MAE-B 237, P.O. Box 116300
Gainesville, FL 32611
Tel.: +1-352-392-9480
Fax: +1-352-392-1071
E-mail: yueling@ufl.edu

A. Haselbacher
Institute of Energy Technology
ETH Zürich, 8092 Zrich, Switzerland

S. Balachandar
Department of Mechanical and Aerospace Engineering
University of Florida, Gainesville, FL 32611, USA

F. M. Najjar
Lawrence Livermore National Laboratory
Livermore, CA 94550, USA

D. S. Stewart
Department of Mechanical Science and Engineering
University of Illinois, Urbana, IL 61801, USA

1 Introduction

Adding reactive metal particles into condensed phase explosive has become a common approach to increase the total energy release of an explosive system [9, 43, 44]. When a detonation wave propagates through explosive reactants, chemical reactions occur. Explosives turn into high-pressure and high-temperature gaseous products, which expand outward rapidly. Metal particles gain significant velocity and their temperature rises due to interaction with the detonation wave. The detonation-particle interaction can also melt and ignite the metal particles. As the reaction rate of metals is slower than the explosive, the embedded metal particles are dispersed due to the initial detonation and they will continue to burn and release energy. The energy from post-detonation burning of particles can significantly enhance the sustained impulse delivered by the blast wave. This enhancement effect of metal particles has been observed in experiments and also practical applications [43]. It is clear that the interaction between the detonation wave and the metal particles plays an important role in the overall process [33, 45]. This interaction determines the initial velocity and temperature of the metal particles. The breakage and fragmentation of the particles are closely related to the peak force exerted on the particles during detonation-particle interaction (DPI). Similarly, ignition of the particles depends on the peak heating. Even otherwise, the initial momentum and energy transferred to the particles have a strong influence on their later time evolution [15]. If the detonation-particle interaction process is not accurately captured, we will not be able to predict the long time evolution or the enhanced effects of metal particles.

A detonation wave can be considered as a very strong shock wave accompanied with chemical reactions. Understanding of particle interaction with a strong shock wave is thus a good approximation. Experimental study for particle interaction with a shock wave is challenging. Nevertheless, some previous experiments for solid particles interacting with a shock wave in gas flows have been reported recently [36, 37, 46]. In most of the previous works for shock-particle interaction, the shock strength is weak compared with the material strength of particle. Therefore, the particle can be considered as rigid and complex physics such as compression heating can be neglected. Here we are interested in the problem of a strong shock interacting with a particle, where the shock strength is of sufficient magnitude that the deformation and the compression of the particle cannot be ignored. In particular, we are interested in the problem of detonation-particle interaction in the context of condensed explosive detonations, where the density of the products of detonation is substantial and the post-shock pressure can be significantly larger than the yield strength of particle. Experiments of shock interaction with deformable particles (SIDP) in the context of metal particles subjected to an intense shock in a condensed matter ambience are limited in the literature, due to the complex nature of such experiments [9, 10, 44].

At the enhanced post-shock pressure of a detonation process both the particle and the embedding condensed matter behave like compressible fluids and simulations of a strong shock interacting with a particle can be performed using Euler equations for both the particle and the ambient medium [33, 45]. The key to performing such SIDP simulations is rigorous models for material properties of the particle and the ambient medium. Properties of the condensed matter, such as Hugoniot loci, are generally provided by experiments. By employing experimental data/correlations of material properties, previous simulations by Zhang et al. [45], Ripley et al. [34], and Ripley [33] have shown the capability to capture SIDP in condensed matter. In the above efforts, fully resolved direct numerical simulations (DNS) at the microscale were per-

formed to investigate the interaction of a planar shock/detonation wave with a single or a small number of spherical metal particles. However, in practical applications involving a very large number of particles, it is impractical to resolve the deformation of particles and the flow at particle scale. Instead, a point-particle approach (PPA) must be used [1], in which particles are modeled as point masses. As the microscale details of shock interaction with the deformable particles are not resolved in PPA, the momentum and energy transfer between particles and the ambient medium must be given by proper interphase coupling models.

We note that shock interaction with a deformable particle (SIDP) occurs in other applications as well. For example, shock interaction with a droplet or a bubble can lead to significant deformation of the droplet or the bubble. In fact a sufficiently strong shock can lead to violent breakup and fragmentation of the droplet or bubble, [4, 25, 31]. Also, shock or blast interaction with deformable soft materials, such as biological tissues, is of great recent interest [38]. The present modeling and simulation effort will be limited to only modest particle deformation and will not include complex scenarios such as breakup and fragmentation.

Recently, Parmar et al. [27–30] and Ling et al. [14–16] proposed physics-based interphase coupling models for momentum and energy exchange between particles and gas in compressible particle-laden flows. The key feature of the models is that unsteady force and heating contributions are included in the overall momentum and energy coupling. The models were validated against experimental data and fully resolved DNS results [16, 27, 28]. The models were applied to shock-particle interaction problems in both planar and spherical configurations [14, 15]. Unsteady contributions were observed to be significant compared to the quasi-steady contributions for a wide range of particle density and diameter.

The overarching goal of this paper is to extend the above models to account for the effects of particle deformation and compression heating, so that the improved model can be used in macroscale simulations where SIDP is involved. We will first describe the flow field arising from SIDP in section 2. The key parameters determining the shock refraction pattern will be discussed. Then in section 3, we analyze the overall interaction process through time-scale analysis. It will be shown that SIDP can be divided into inviscid and viscous phases according to the dominant mechanisms. From modeling perspective, the inviscid phase is more challenging. Most of the complicated physics, such as shock reflection and refraction, particle deformation, and compression heating, occur during the inviscid phase. The multiphysics hydrodynamic code, ALE3D, developed by Lawrence Livermore National Laboratory is used to simulate the details of SIDP during the inviscid phase. The simulation approach and the DNS results will be discussed in section 4. Then we will describe the present interphase coupling models for SIDP in section 5. Results of the models will be compared with the DNS results and those from standard drag and heat-transfer correlations in section 6. For the purpose of validation, we also apply the model to investigate particle interaction with a Chapman-Jouguet (CJ) detonation wave, and compare the results of the present model with the corresponding DNS results presented in [33]. Finally, we will draw conclusions in section 7.

2 General analysis and key parameters

When a very strong shock wave interacts with a solid particle, and in particular when the post-shock pressure is much higher than the material yield strength of the particle, both the particle and the ambient medium can be taken to behave as inviscid compressible fluids. In such problems, Euler equations are often used to repre-

sent both the particle and ambient medium [45]. This approach employs a very simple model, but yet it is generic and powerful enough to be useful in a wide range of problems of interest. This approach does not place any *a priori* restriction on the phase of the particle or the ambient medium. In the present context of a metal particle embedded in a condensed matter and subjected to an intense shock wave, the particle is a solid, while the ambient medium can be a solid or a liquid. In the case of a droplet subject to a strong shock, the deformable "particle" is the droplet and the ambient medium can be a liquid or solid. The problem of shock-bubble interaction (SBI) has also been intensely studied (see [32]) and in this case the deformable "particle" is the gas bubble, which again can be embedded in an ambient medium of another gas or as in the familiar case of an air bubble subjected to a shock wave propagating through water, the ambient medium can be a liquid. Other combinations of particle and ambient phases are also possible. For example, in the problem of shock-induced pore collapse and ignition initiation in a condensed phase reactive material [22], the ambient medium is a solid and the deformable "particle" is an air or gas pocket. Thus the terms "particle" and "ambient medium" are used in a broad sense, with the understanding that their phases can be either gas, liquid or solid.

The generic feature common to all the above problems is that a particle of finite size embedded in an ambient medium of different material, deforms, translates and heats up when subjected to an intense shock propagating through the ambient medium. Since the particle and the ambient medium are of different materials, the interaction of the shock wave with the particle will generate a complex flow field, including shock-wave transmission, refraction and reflection, along with possible vorticity production and transport. The details of this complex interaction on one hand depend on the shape and size of the particle and also on the intensity of the shock wave. In addition, the nature of the shock interaction with the deformable particle will critically depend on the material properties of both the particle and the ambient medium. For example, in the case of shock propagation over a gas-gas interface, due to the miscibility of the materials, long term evolution can be influenced by interfacial turbulence and mixing. Also, the details of shock-bubble interaction in the gas-liquid context can be qualitatively different from that of a metal particle embedded in a condensed phase reactive material (see [25] and [45]). In this work our primary attention is to the later scenario. Furthermore, we will restrict attention to only small spherical particles of diameter a few microns to few millimeters.

2.1 Shock impedance ratio

There are two key parameters that determine the overall qualitative features of SIDP. They are the shock impedance ratio Z_1^p/Z_1^a and the shock speed ratio u_{st}^p/u_{si}^a. Here the superscripts p and a correspond to the particle and the ambient medium, respectively. The subscripts si and st represent the incident and transmitted shocks, and thus u_{si}^a and u_{st}^p denote the propagation velocities of the incident shock traveling in the ambient medium and the transmitted shock traveling in the particle, respectively. When a shock wave interacts with an interface separating different materials, the transmitted wave remains a shock wave, while the reflected wave can be a shock wave or an expansion fan. The reflected wave pattern is determined by the shock impedance across the interface. The shock impedance ratio for an interface of two ideal gases can be expressed as (see [11])

$$\frac{Z_1^p}{Z_1^a} = \frac{\rho_1^p c_1^p}{\rho_1^a c_1^a} \left\{ \frac{\frac{1}{2\gamma^p}\left[(\gamma^p+1)\frac{p_2^p}{p_1^p} + (\gamma^p-1)\right]}{\frac{1}{2\gamma^a}\left[(\gamma^a+1)\frac{p_2^a}{p_1^a} + (\gamma^a-1)\right]} \right\}^{1/2}, \tag{1}$$

where $(\rho_1^p, c_1^p, \gamma^p)$ and $(\rho_1^a, c_1^a, \gamma^a)$ denote the pre-shock density, speed of sound, and specific heat ratio of the particle and ambient medium, respectively. The pressure behind the incident shock traveling in the ambient medium is represented by p_2^a; while the pressure behind the transmitted shock traveling in the particle is represented by p_2^p. The pre-shock pressure for the particle, p_1^p, is taken to be the same as that in the ambient medium, p_1^a. The pre-shock and post-shock states are indicated by subscripts 1 and 2, respectively. When the impedance ratio $Z^p/Z^a < 1$, the reflected wave is an expansion fan; when $Z^p/Z^a > 1$, the reflected wave is a shock wave. This simple criterion applies only for the case of a planar shock impinging normally on a planar material interface. In case of oblique interaction or curved shocks and material interfaces, additional complexities arise. For the case of a spherical particle, the material interface is clearly non-planar. Nevertheless, the simple criterion based on shock impedance ratio applies near the front of the particle and dictates the character of the initial reflected wave pattern near the front of the particle.

Unfortunately, shock impedance and the ratio in Eq. (1) depend not only on the material properties on either side of the interface, but also on the shock strength, parameterized by the pressure jump across the shock. In the limit of a weak incident shock $p_2^a/p_1^a \to 1$, the resulting transmitted shock will also be weak $p_2^p/p_1^p \to 1$ and the shock impedance ratio can be approximated by the acoustic impedance ratio

$$\left.\frac{Z_1^p}{Z_1^a}\right|_{p_2^a/p_1^a \to 1} = \frac{\rho_1^p c_1^p}{\rho_1^a c_1^a}\,. \tag{2}$$

In both Eqs. (1) and (2) the material properties are to be taken under undisturbed conditions before the arrival of the shock wave. Thus, the advantage of the above acoustic limit is that it depends only on the thermodynamic properties of the particle and the ambient medium. As a result, the nature of the reflected wave in shock interface interaction is often estimated based on the acoustic impedance ratio, instead of the true shock impedance ratio. However, it should be noted that this simplification under certain conditions can lead to erroneous estimation.

A more appropriate condition for the present consideration is when the incident shock strength is very large and therefore we consider the limit $p_2^a/p_1^a \gg 1$. Correspondingly the transmitted shock is also very strong and we can set $p_2^p/p_1^p \gg 1$. Under this condition the shock impedance ratio can be expressed as

$$\left.\frac{Z_1^p}{Z_1^a}\right|_{p_2^a/p_1^a \to \infty} = \frac{\rho_1^p c_1^p}{\rho_1^a c_1^a}\left[\frac{\gamma^a(\gamma^p+1)p_2^p/p_1^p}{\gamma^p(\gamma^a+1)p_2^a/p_1^a}\right]^{1/2}\,. \tag{3}$$

Although, the shock impedance ratio still depends on p_2^a/p_1^a and p_2^p/p_1^p, the demarcation between reflected shock and reflected expansion wave requires only the condition $(Z_1^p/Z_1^a)_{p_2^a/p_1^a \to \infty} = 1$. In this limit of matching impedance, we also have the transmitted shock being equal to the incident shock and as a result $p_2^p/p_1^p = p_2^a/p_1^a$. Thus, in the limit of a very strong incident shock, the reflected wave pattern, i.e., a shock wave or an expansion fan, can be estimated, without the precise knowledge of the actual shock strength, in terms of the following simple condition

$$\frac{\rho_1^p c_1^p}{\rho_1^a c_1^a}\left[\frac{\gamma^a(\gamma^p+1)}{\gamma^p(\gamma^a+1)}\right]^{1/2} \gtrless 1\,. \tag{4}$$

Here again the criterion depends only on the material properties of the particle and the ambient medium.

2.2 Shock speed ratio

The second parameter of relevance is the ratio of the speed of the transmitted shock to that of the incident shock. When the materials on both sides of the interface can be represented as ideal gases, and in the case of a normal shock

propagating through a planar interface, the ratio of transmitted to incident shock speed can be written as

$$\frac{u^p_{st}}{u^a_{si}} = \frac{c^p_1}{c^a_1}\left[\frac{1+\dfrac{\gamma^p+1}{2\gamma^p}(\dfrac{p^p_2}{p^p_1}-1)}{1+\dfrac{\gamma^a+1}{2\gamma^a}(\dfrac{p^a_2}{p^a_1}-1)}\right]^{1/2}, \qquad (5)$$

The shape of the transmitted shock in a spherical particle can be determined by this shock speed ratio. When $u^p_{st}/u^a_{si} > 1$, the incident shock far away from the particle is moving slower than the transmitted shock passing through the particle. As a result, shock refraction is divergent, and the transmitted shock has convex curvature, see Fig. 1(b). If $u^p_{st}/u^a_{si} < 1$, the transmitted shock propagates slower than the incident shock, then the shock refraction is convergent, and the transmitted shock has a concave curvature, see Fig. 1(a).

In the acoustic limit of weak incident and transmitted shocks, their propagation speeds are just the speed of sound in the respective medium. Thus, in this limit the sound speed ratio being greater than or less than one determines the shapes of the transmitted and the refracted shocks. Of more relevance here is the limit of very strong incident and transmitted shocks (i.e., $p^a_2/p_1 \gg 1$ and $p^a_2/p_1 \gg 1$). In this limit, as discussed above for the impedance ratio, the criterion for estimating the structure of the transmitted shock, i.e., to be convex or concave, and the refraction pattern of the shock within the particle, i.e., to be divergent or convergent, is given by

$$\frac{c^p_1}{c^a_1}\left[\frac{\gamma^a(\gamma^p+1)}{\gamma^p(\gamma^a+1)}\right]^{1/2} \gtrless 1\,. \qquad (6)$$

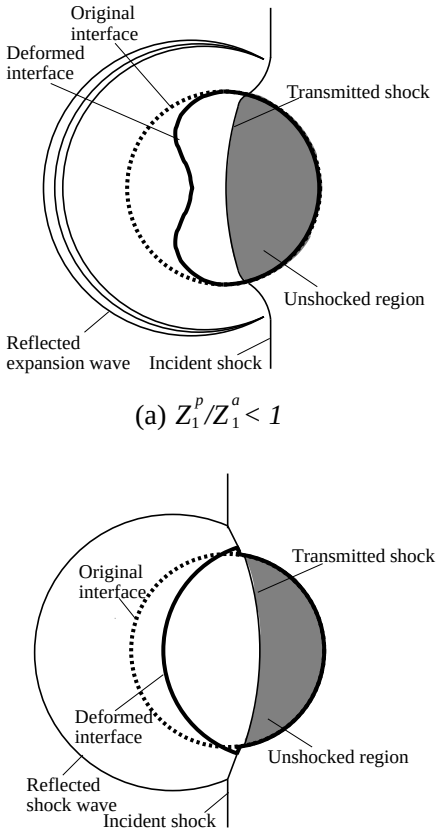

Fig. 1 Representative schematic of shock-particle interaction flow field.

2.3 Gas systems vs condensed-matter systems

The shock interaction behavior in gas-gas systems and those of condensed matter systems differ and the difference can be related in terms of differences in their shock impedance and shock speed ratios. For gases obeying ideal gas law, in general, if the particle is denser (lighter) than the ambient medium, then the corresponding speed of the transmitted wave within the particle is slower (faster) than the incident wave speed in the ambient medium. Also, the impedance of the particle in general will be larger (smaller) than that of the ambient medium. Thus, in a shock-bubble interaction problem, if the gas bubble is denser (lighter) than the surrounding gas then the reflected shock in general can be expected to be a shock (expansion fan) and the re-

fracted shock pattern around the particle will be convergent (divergent) [32]. In condensed matter the general behavior is often reversed. The acoustic speed in a denser particle is often faster and correspondingly the impedance is larger. However, the above generalizations are based on acoustic limit and assume specific heat ratios to be nearly invariant. Thus, even in cases involving real gases one must accurately compute the shock impedance and shock speed ratios to estimate the reflected and the refracted wave behaviors. In case of condensed matter systems, we can still take the shock impedance and shock speed ratios to accurately predict the shock-particle interaction behavior. However, the behavior of condensed matter may depart from the ideal gas law and thus the relations presented above for impedance and shock speed ratios will not be strictly applicable.

2.4 Particle deformation

Another important feature of shock interaction with a deformable particle is vorticity production and its influence on interface deformation. In shock-particle interaction, vorticity is generated due to baroclinic mechanism arising from misalignment of the pressure and the density gradients. Initially, since the flow ahead of the shock wave is stagnant and the shock wave is planar, vorticity is zero everywhere. During the short duration of initial shock-particle interaction viscous effects are negligible and baroclinicity is the primary source for vorticity production [32]. The direction of rotation of vorticity is determined by the orientation of the density gradient at the interface. In Figs. 1 (a) and (b), the rotation is counter-clockwise and clockwise in the upper half plane, respectively. Vorticity generation is related to interface deformation during the interaction and its final shape after the passage of shock wave.

The degree of deformation the particle undergoes when subjected to a shock depends on both the shock impedance ratio Z_1^p/Z_1^a and the shock strength. When shock impedance is nearly matched $Z_1^p/Z_1^a \approx 1$ or when the shock is weak, deformation will be small. Under such condition, for example, a spherical particle may be only slightly compressed along the shock propagation direction and may end up oblate spheroidal in shape. If $Z_1^p/Z_1^a \ll 1$ or $\gg 1$ or if the shock is strong, then the particle may undergo significant deformation. The particle interface can roll up and the particle can tear apart. The forces exerted on a particle dictate its deformation, which in turn influences the overall force exerted on the particle. Therefore, the effect of particle deformation needs to be considered in force modeling. Here we are concerned with the regime where the particle undergoes substantial deformation, but it maintains integrity and thereby we will not address issues such as fracture and fragmentation.

3 Time scale analysis

3.1 Overall interaction process

Before we investigate the important time scales of the problem we first examine the sequence of key events that follows shock interaction with a deformable particle. When a spherical particle interacts with a planar shock wave with constant post-shock properties, the overall process can be represented by Fig. 2. The incident shock wave travels from left to right with constant speed u_{si}^a and encounters an initially stationary particle. As a result of this interaction the particle is rapidly accelerated forward, its temperature increases due to heating, and the particle undergoes deformation. The schematic in Fig. 2 is drawn in a frame attached to the shock and in this frame of reference the particle moves from right to left. Before the arrival of the shock wave, the particle is stationary and in thermal equilibrium with the ambient medium (state (a)), i.e., $u^p = 0$ and $T^p =$

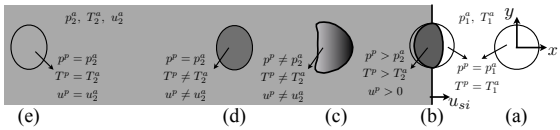

Fig. 2 Schematic of shock wave interaction with a spherical particle.

T_1^a. When the shock wave reaches the particle, complex interaction described in Fig. 1 occurs (state (b)). The portion of particle swept through by the transmitted shock is accelerated and heated, i.e., $u^p > 0$, $T^p > T_1^a$ and $p^p > p_1^a$. At state (c), the transmitted shock has completely passed through the particle, but reflected waves generated at the interface due to their impedance mismatch, continue to travel back and forth inside the particle. As a result, the velocity, temperature, and pressure inside the particle are non-uniform and different from those of the ambient medium behind the incident shock. As time evolves, with each internal reflection within the particle the flow field inside the particle becomes weaker and weaker, and the pressure within the particle first equilibrates to the post-shock ambient pressure, i.e., $p^p = p_2^a$. During this initial stage, the dominant mechanism of particle evolution is inviscid, and the viscous and diffusive effects are negligibly small.

We denote this intermediate equilibrium state as the *inviscid quasi-equilibrium state* and is schematically represented by state (d) in Fig. 2. At this stage the velocity inside the particle is nearly uniform, but the particle velocity in general will differ from the post-shock ambient velocity. Similarly, the particle, although heated by shock-induced compression, will not be the same as the post-shock ambient temperature. This intermediate inviscid equilibrium state is denoted with subscript 3 in the velocity and temperature evolution plots presented in Fig. 3. It should be noted that temperature may still be non-uniform inside the particle at this stage. As

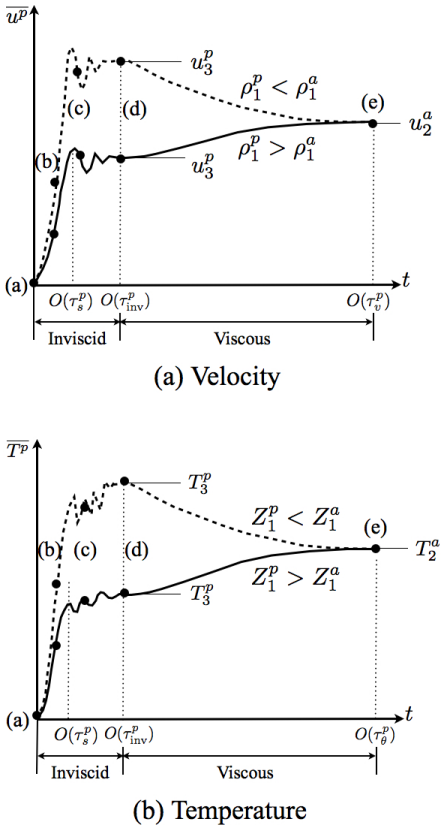

Fig. 3 Schematic of time evolutions of particle average (a) velocity and (b) temperature in the interaction with a shock wave.

time continues to evolve, viscous and diffusion mechanisms become important, which eventually bring the particle velocity and temperature to be in equilibrium with the post-shock ambient medium, i.e., $u^p = u_2^a$ and $T^p = T_2^a$. The final state represents the *viscous equilibrium state* and is denoted as (e) in Fig. 2. Since we consider situations in which post-shock pressure exceed the elastic limit of particle material, the deformation of the particle is irreversible.

3.2 Time scales in SIDP

In the process of shock-particle interaction, there are multiple time scales that dictate the overall time evolution of particle velocity and temperature. A schematic of the time evolution of mean particle velocity and temperature is shown in Fig. 3. Different states shown in Fig. 2 are also indicated in Fig. 3. The first is the duration of shock passage through the particle. This is the time it takes from the instance the incident shock contacts the particle to when the transmitted shock completely passes out of the particle. This time scale is defined as the *shock-particle interaction time*,

$$\tau_s^p = \frac{d^p}{u_{si}^a} \,. \tag{7}$$

where d^p is the particle diameter. Strictly speaking, the transmitted shock speed u_{st}^p instead of the incident shock speed u_{si} should be used to calculate τ_s^p. But since u_{st} varies with particle material, we use u_{si} here for simplicity. Because u_{st} and u_{si} are of the same order of magnitude, u_{si} is sufficient to estimate the particle-shock interaction time scale. As can be seen from Fig. 3 during $0 < t < \tau_s^p$, the mean particle velocity and temperature increase rapidly.

The second time scale is the *inviscid time scale* for the particle to reach pressure equilibrium with ambient medium i.e., $p^p = p_2^a$, see state (d) in Fig. 2. This time scale is denoted as τ_{inv}^p, as for $t < \tau_{\text{inv}}^p$ viscous effect is negligible and the flow can be considered inviscid. When the transmitted shock reaches the interface with the ambient medium, the impedance mismatch will generate reflected waves which will travel back into the particle. Similar wave-interface interaction happens when the reflected wave reaches the particle interface. During $\tau_s^p < t < \tau_{\text{inv}}^p$, these reflected waves move back and forth inside the particle until they eventually become negligibly weak. Typically by about $O(10)$ or so reflections, the pressure equilibrium is nearly achieved. Therefore, it can be expected that τ_{inv}^p is a multiple of the shock-particle interaction time scale, i.e., $\tau_{\text{inv}}^p \approx 10\tau_s^p$. A more precise estimate of τ_{inv}^p will depend on material properties and shock strength. At around τ_{inv}^p, the mean particle velocity and temperature will reach their intermediate asymptotic values, u_3^p and T_3^p.

Only for times much longer than τ_{inv}^p, the viscous and thermal diffusion effects become important in the momentum and energy transfer. On this longer time scale the viscous drag force and the conductive/convective heat transfer mechanisms will become significant to bring the particle velocity and temperature to the post-shock ambient values of u_2^a and T_2^a. The time scale for u^p to reach u_2^a is the particle mechanical response time

$$\tau_v^p = \frac{\rho^p (d^p)^2}{18\mu^a} \,, \tag{8}$$

and that for T^p to reach T_2^a is the thermal response time

$$\tau_\theta^p = \frac{\rho^p C^p (d^p)^2}{12 k^a} \,. \tag{9}$$

In the above equations, μ^a and k^a are the viscosity and thermal conductivity of the ambient medium. The particle heat capacity is denoted by C^p. Typical values of these time scales can be obtained by using the following sample values appropriate in the context of shock-particle interaction in condensed material: $\rho^p \sim O(10^3\ \text{Kg/m}^3)$, $\mu^a \sim O(10^{-5}\ \text{Pa s})$, $u_s \sim O(10^3\ \text{m/s})$, and $d^p \sim O(1\ \mu\text{m})$. Since thermal diffusivity $k/(\rho C^p)$ is typically $O(1)$, the thermal response time is of the same order as the mechanical response time. But more importantly, the mechanical and thermal response times are about three to four orders of magnitude larger than τ_s^p. Therefore, the overall shock-particle interaction process can be divided into two phases according to the dominant mechanism: the inviscid-phase and the viscous-phase. The inviscid-phase lasts from $t = 0$ to about τ_{inv}^p, and the viscous-phase from τ_{inv}^p to when particle reaches its me-

chanical and thermal equilibrium with the ambient medium.

4 DNS of inviscid-phase of SIDP

4.1 Governing equation and simulation approach

In this section, we investigate the interaction between a spherical particle and a non-reacting shock wave through direct numerical simulations. Since post-shock pressure is in excess of the yield strength, both the particle and the ambient medium are treated as compressible fluids. The governing equations are conservation of mass, momentum, and energy, written as follows:

$$\frac{D\rho}{Dt} = -\rho\nabla\cdot\mathbf{u}\,, \tag{10}$$

$$\rho\frac{D\mathbf{u}}{Dt} = \nabla\cdot\sigma\,, \tag{11}$$

$$\rho\frac{DE}{Dt} = \nabla\cdot(\sigma\cdot\mathbf{u})\,, \tag{12}$$

where ρ, $\mathbf{u}$, E, and σ represent density, velocity, total energy, and stress tensor, respectively. Symbols without superscripts represent properties corresponding to both the particle and the ambient medium. The substantial derivative denoted as D/Dt is defined as

$$\frac{D}{Dt} = \frac{\partial}{\partial t} + \mathbf{u}\cdot\nabla\,. \tag{13}$$

Since we only consider the inviscid-phase of SIDP, viscous effects are ignored and thus σ reduces to $-p\mathbf{I}$.

To close the equation system (10)-(12), the Mie-Grüneisen equation of state (EOS) is employed:

$$p(\rho,e) = p_H(\rho) + \rho\Gamma(e - e_H(\rho))\,, \tag{14}$$

where e is internal energy, Γ is the Grüneisen coefficient, and $p_H(\rho)$ and $e_H(\rho)$ are pressure and internal energy along the Hugoniot curve, respectively. To solve Eqs. (10)-(12), Eq. (14) is sufficient. However, as we also want to solve for particle temperature, the following Mie-Grüneisen thermal equation of state is also needed:

$$T(\rho,e) = T_H(\rho) + \frac{e - e_H(\rho)}{C_v}\,, \tag{15}$$

where C_v is specific heat at constant volume, which is considered as constant here. The Hugoniot curve is approximated by the linear $u_s - u_2$ relation:

$$u_s = c_1 + su_2\,, \tag{16}$$

where u_s, c_1, and u_2 are the shock speed, pre-shock speed of sound, and post-shock velocity. The coefficient s is determined by shock-compression experimental data. Based on Eq. (16), the expressions of $p_H(\rho)$ and $e_H(\rho)$ can be derived from conservation laws. For $T_H(\rho)$, the method of [41] is used, in which C_v and $(\partial p/\partial T)_v$ are considered as constants.

The evolution equations for conservation of mass, momentum, and energy, Eqs. (10)-(12), are solved in an Eulerian framework on a structured mesh. Axisymmetry was used to optimize computational resources. The multiphysics code, ALE3D [24], was used to perform these simulations. The mathematical formulation is based on an operator-split method and invokes an arbitrary Lagrangian-Eulerian (ALE) approach in the 2-D axisymmetric configuration.

The capabilities available in ALE3D allow solving the evolution equations either in a pure Lagrangian, pure Eulerian, or in an ALE manner. Within an Eulerian or ALE construct, a remap formalism is invoked, allowing the advection of the conserved variables on the moving mesh. In order to simulate hydrodynamic flow across shock waves, it is necessary to add some form of numerical dissipation to the conservation equations, such as the artificial viscosity technique by von Neumann and Richtmyer [40].

The governing equations are discretized using a finite-element method and are solved in a weak form. To control numerical instabilities

due to the finite-element formulation, hour-glass mode control is invoked. The spatial discretization is of hybrid form where the node coordinates and velocities are node-centered variables; while the density, pressure, internal energy, temperature are cell-centered quantities. The basis function consists of bi-linear and piecewise constant for the velocities and pressure, respectively. The time integration approach follows a staggered explicit formulation, where the velocity fields are computed in a staggered manner from the zonal state variables. Thus, the Lagrangian coordinates, accelerations, pressure, energy, and mass are centered in time at t^n; while the velocities, are centered in time at $t^{n-1/2}$.

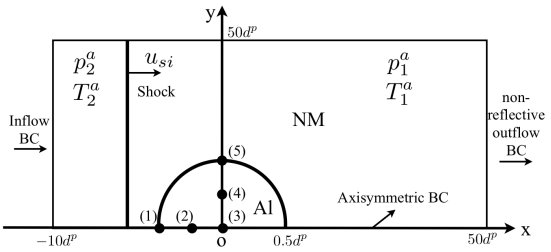

Fig. 4 Schematic of DNS computational domain.

	NM	Al
ρ_1[Kg/m^3]	982	2785
T_1[K]	298	298
c_1[m/s]	1647	5350
s	1.637	1.350
C_v[J/(Kg K)]	920.5	1733

Table 1 Properties of nitromethane (NM) and aluminum (Al).

	Case 1	Case 2
u_{si}[m/s]	2900	4800
u_2^a [m/s]	1000	2270
p_2^a[GPa]	2.84	10.7
ρ_2^a[Kg/m^3]	1507	1861
T_2^a[K]	585	1745
a_2^a[m/s]	3200	5730

Table 2 Summary of shock conditions for DNS cases.

4.2 Simulation results

A schematic of the computational domain is shown in Fig. 4. The flow is taken to be axisymmetric about $y = 0$ axis. The computational domain extends in the x-direction from x/d^p=-10 to x/d^p=+50 where the particle center is located at (0,0); while in the y-direction, the domain length is $+50d^p$. An inflow boundary condition is imposed on the left boundary; while non-reflective outflow condition on the right boundary. On the top boundary, the y-velocity and the gradient of x-velocity are taken to be zero. The grid size is uniform in the x-direction and $\Delta x/d^p$ is set to be 0.01. In y-direction, a uniform mesh is invoked in the particle vicinity, i.e., $\Delta y/d^p = 0.01$ for $0 \leq y/d^p \leq 8$, then the mesh is smoothly stretched toward the top boundary. The total mesh consists of 1.5M cells. A mesh resolution study has been performed and it showed that the present grid size minimizes computational resources while being mesh-independent. The time step size is computed based on a CFL condition of 0.5.

In the simulations, the ambient and the particle materials are take to be nitromethane and aluminum, respectively. The particle is initially stationary and located at $x = 0$. A non-reacting shock wave propagates from left to right, which first contacts the particle at $t = 0$. The pre-shock properties and Hugoniot properties of both nitromethane and aluminum are listed in Table 1. Two cases with different shock strengths are considered here. The shock speed and post-shock conditions are listed in Table 2

4.2.1 Flow field arising from SIDP

The density contour at $t/\tau_s = 8.7$ for Case 1 is shown in Fig. 5. At this time, the shock wave has passed through the particle. We observed

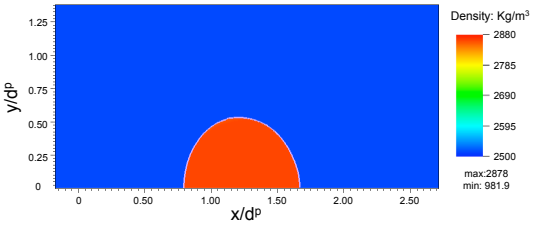

Fig. 5 Density contour at $t/\tau_s = 8.7$ showing the final shape of the aluminum particle after the shock passage for Case 1.

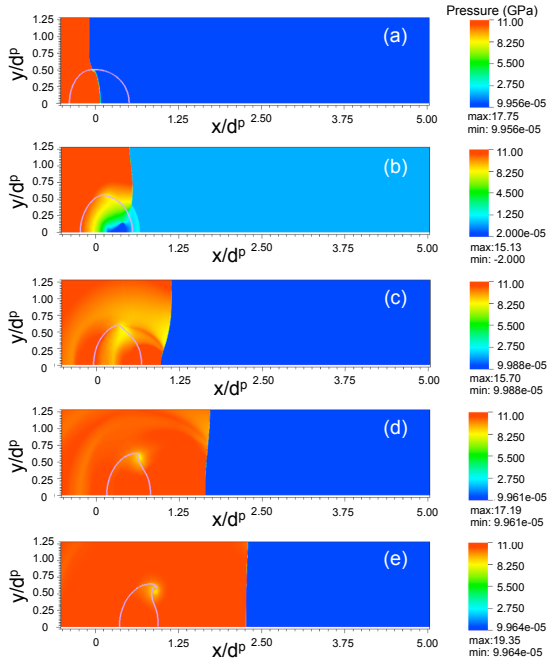

Fig. 6 Pressure evolution in SIDP for Case 2. (a) $t/\tau_s = 0.4$, (b) $t/\tau_s = 1.0$, (c) $t/\tau_s = 1.6$, (d) $t/\tau_s = 2.2$, and (e) $t/\tau_s = 2.8$.

that the aluminum particle has reached the inviscid quasi-steady equilibrium state (State (d) in Fig. 2). The aluminum particle and the ambient nitromethane have reached pressure equilibrium. The velocity and temperature of the aluminum particle reach constant values, but they are different from those of the ambient medium: $\overline{u^p}/u^a = 0.58$ and $(\overline{T^p} - T_1^a)/(T_2^a - T_1^a) = 0.15$. This indicates that the aluminum particle has gained significant momentum and energy from the inviscid interaction with the shock wave. The final shape of the aluminum particle can also be seen in Fig. 5. Due to the interaction with the shock wave, the particle is compressed along the streamwise direction, changing from a sphere to an oblate-spheroid-like shape.

The time evolutions of the pressure and temperature contours for Case 2 are shown in Figs. 6 and 7. The shock refraction pattern is seen to be consistent with the schematic in Fig. 1 (b), as the shock impedance of aluminum is larger than nitromethane. The transmitted shock in the aluminum particle propagates faster than the incident shock in the ambient nitromethane, resulting in a convex shock shape. When the transmitted shock wave reaches the downstream edge of the particle, another shock refraction occurs. According to the analysis in section 2, the shock refraction will generate a transmitted shock and a reflected expansion fan. But due to the spherical geometry, the flow field is more complex than 1D case. The incident shock that diffract over the particle is seen to overtake the transmitted shock and the two shocks eventually merge together. It can be seen that at about $t/\tau_s = 2.8$, the shape of the main shock wave returns back to nearly planar. The reflected expansion waves propagates upstream back into the particle and interact with the particle interface again. These subsequent interactions and the generated waves are seen to be quite complex, but the waves decay fast.

Similar to Case 1, the particle is compressed in the streamwise direction for Case 2. However, due to the higher shock strength in Case 2, the particle compression is stronger and results in a sharp edge which was not seen in Case 1. It is observed that this sharp edge induces flow separation downstream of it at later times, see Figs. 6 (d) and (e). The flow separation seems

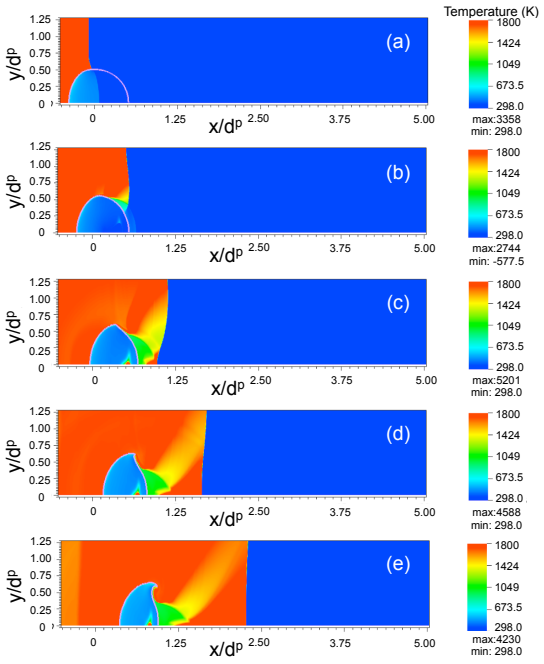

Fig. 7 Temperature evolution in SIDP for case 2. (a) $t/\tau_s = 0.4$, (b) $t/\tau_s = 1.0$, (c) $t/\tau_s = 1.6$, (d) $t/\tau_s = 2.2$, and (e) $t/\tau_s = 2.8$.

to contribute to the continuous deformation of the particle after the shock passage.

From Fig. 7, it can be seen that the temperature inside the aluminum particle increases significantly due to the interaction with the shock wave. As the transmitted shock passes through the particle, e.g., at $t/\tau_s = 0.4$, the post-shock temperature of aluminum particle reaches about 580K. Though the post-shock temperature of the particle is still lower than in the ambient nitromethane, compared to the initial temperature, the aluminum particle is significantly heated. After the passage of the initial shock wave, the subsequent wave interactions continue to change the temperature of the particle. Due to the complexity of the subsequent wave interactions, the temperature field inside the particle is non-uniform.

4.2.2 Evolutions of Lagrangian tracers within the particle

In order to closely investigate the complex flow field, we trace five material points that are initially located within the aluminum particle and follow their positions and local thermodynamic properties in the Lagrangian framework. The initial positions of these tracers are indicated in Fig. 4. The time evolutions of pressure and temperature of these five tracers for case 1 are shown in Fig. 8.

The general trends of pressure evolutions for the different tracers are quite similar. The pressure of each tracer increases rapidly when the transmitted shock reaches the tracer. After that the tracer pressure drops and rises multiple times until it approaches the asymptotic value p_2^a. It can be seen that at about $t = 4\tau_s$ all tracers almost reach p_2^a.

We observe that the tracer pressure decreases following the passage of the transmitted shock. This is different from the one-dimensional analogue of shock-particle interaction, i.e., when a planar shock wave interacts with a planar material interface as shown in Fig. 9. Here, the post-transmitted-shock pressure within the particle will remain constant until the transmitted shock reaches the right-edge of the 1D particle. More details on a planar shock interacting with an 1D particle can be found in [33]. In the spherical-particle case, post-incident-shock pressure of nitromethane on the lateral side of particle is smaller than the post-transmitted-shock pressure inside the aluminum particle. The lateral pressure gradient causes the the shocked portion of particle to expand in the y-direction normal to the direction of shock propagation. It is also interesting to note that this lateral expansion of the shocked portion of the particle is roughly isothermal, see Fig. 8(b).

For tracers 3 to 5, which are initially located along the y axis, it can be seen that the post-transmitted-shock pressure is quite close. But

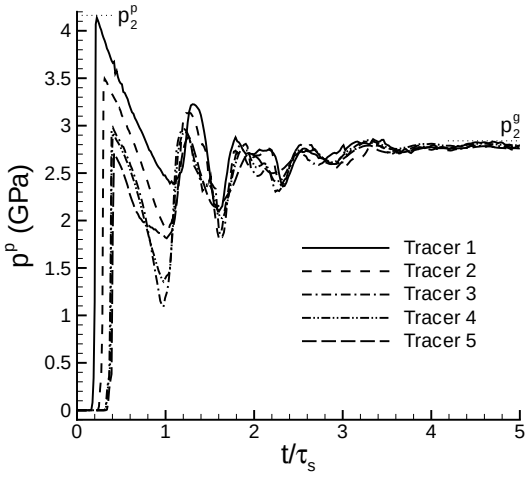

(a) Pressue

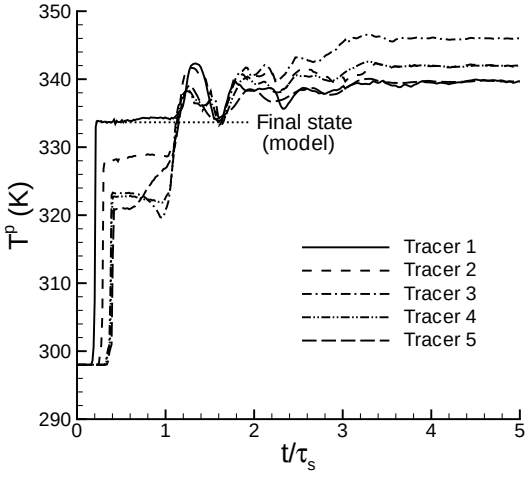

(b) Temperature

Fig. 8 Time evolutions of pressure and temperature of the five tracers inside the particle for case 1.

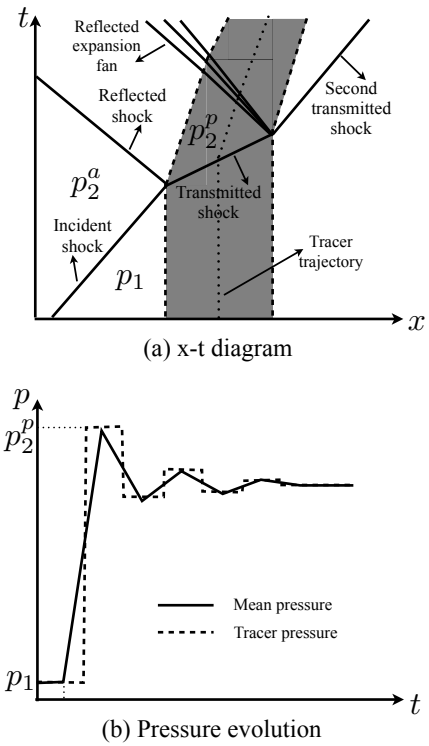

Fig. 9 Schematic of (a) x-t diagram for a nitromethane non-reacting shock wave interacting with a 1D aluminum particle and (b) time evolution of pressure inside the particle.

for tracers 1 to 3, which initially located along the x axis, the post-transmitted-shock pressure decays significantly from tracer 1 to 3, indicating that the strength of the transmitted shock decreases when it propagates inside the particle. It should again be reminded that in the 1D analogue shown in Fig. 9, the transmitted shock speed is constant until it reaches the right-edge of the particle. In the spherical-particle case, the post-transmitted-shock pressure decreases due to lateral expansion, and as a result the transmitted shock slows down. Furthermore, though different tracers reach the same asymptotic pressure, their asymptotic temperatures on the inviscid time scale are different. This is due to the fact that their final pressure was reached through different pressure evolution. In the present case, the difference is around 20% of $(T_3^p - T_1^a)$.

Figure 10 shows variations of tracer density and temperature as functions of tracer pressure. The Hugoniot curve of aluminum corresponding to the initial state (p_1^p, T_1^p, ρ_1^p) is also plotted. First, it can be observed that ρ^p and T^p of all

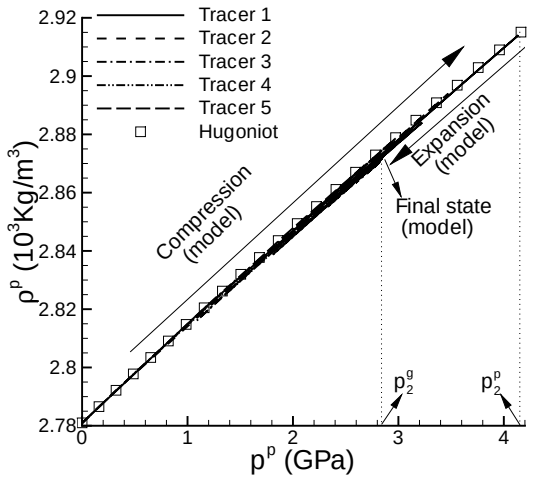

(a) $\rho - p$ diagram

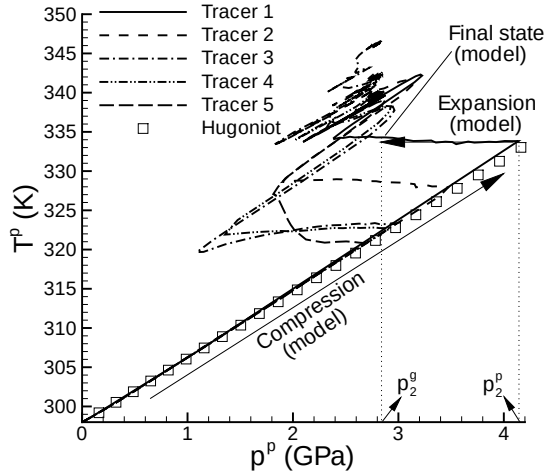

(b) $T - p$ diagram

Fig. 10 Evolutions of density and temperature of the five tracers in $p - \rho$ and $p - T$ diagrams for case 1.

tracers move up along the Hugoniot curve when the transmitted shock wave passes over it. But since the post-transmitted-shock pressure varies between the different tracer, they end up at different points on the Hugoniot curve. When the tracer pressure decreases, ρ^p decreases along a slightly different path. But in general the expansion path on the $\rho^p - p^p$ diagram is pretty close to the Hugoniot curve. Similarly, during the subsequent compression and expansion processes, as the waves internally reflect within the particle, the variation of density along the local pressure stays very close to the Hugoniot curve. As a result, when pressure at the different tracers eventually reach p_2^a, density values at the different tracers are close. Therefore, the value of ρ^p on the Hugoniot curve corresponding to p_2^a, denoted as $\rho_H^p(p_2^a)$, is a good approximation for particle density at the end of inviscid-phase of shock-particle interaction.

Similar to ρ^p, as the initial transmitted shock passes over the different tracer points, T^p increases along Hugoniot curve. However, when pressure decreases after the shock passage, the expansion paths of all the tracers significantly deviate from the Hugoniot curve. It can be seen that T^p varies little in the first expansion. After that, tracer temperature goes up and down with pressure. The paths of the subsequent compression and expansion processes in the $T^p - p^p$ diagram have slopes that are similar to that of the Hugoniot curve corresponding to the first compression. Since the post-transmitted-shock pressure differs between the different tracers, the expansion and compression processes at these Lagrangian tracers are also different. As a result, at the end of the inviscid-phase of shock-particle interaction, though ρ^p and p^p are nearly uniform inside the particle, T^p is not. Therefore, it is challenging to estimate the final average temperature of the particle.

5 Interphase coupling model for SIDP

The results discussed in the above section clearly demonstrate the ability to perform well resolved simulations that capture the details of shock interaction with a deformable particle. Such detailed simulations can be extended to situations involving tens of particles. But the computational cost will be severe, partly because there

are more particles and their interactions with the shock wave needs to be resolved, but more importantly the assumption of axisymmetry cannot be employed and a true three-dimensional simulation is required. Nevertheless, in practical applications involving shock interaction with millions of particles the only viable computational option is the point-particle approach (PPA). In PPA, the details of shock transmission within each particle and the details of defraction around the particles is not faithfully followed. Only the overall effect of particle motion, and its momentum and energy exchange with the ambient medium is computed. Here we want to use the DNS results of the previous section to develop and test a physics-based point particle model that is capable of capturing these averaged behaviors of the particle response accurately.

In a point-particle approach, the Lagrangian evolution equations for a particle are given as

$$\frac{d\overline{x^p}}{dt} = \overline{u^p},\ \frac{d\overline{u^p}}{dt} = f,\ \frac{d\overline{T^p}}{dt} = q\,, \tag{17}$$

where $\overline{x^p}$, $\overline{u^p}$, and $\overline{T^p}$ are the mass averaged position, velocity and temperature of the particle. Note that the bars denote mass averaged quantities over the particle. The overall force divided by the particle mass is denoted by f. Similarly, the overall heating divided by the particle mass and heat capacity is denoted by q. In essence, f and q must be modeled in terms of the incident shock condition and the material properties of the particle and the ambient medium. The resulting closures will be the corresponding interphase coupling models for momentum and energy transfer. It is assumed that the flow remains axisymmetric even as the shock wave interacts with the particle. As a result, the force exerted on the particle is aligned with the direction of shock motion. Since we take gravity to be unimportant compared to the strong hydrodynamic forces, the motion of both the particle and the ambient medium will remain one dimensional at the macroscale (taken to be along the x-coordinate). Therefore, Eq. (17) has been written in one-dimensional form.

To model the momentum and energy transfer between the particle and the ambient medium during shock-particle interaction, we divide the overall force and heating exerted on the particle into contributions from different physically meaningful mechanisms. This is the approach that has been successfully followed in the context of low speed incompressible multiphase flows [6, 18, 20] and we follow the extension of this approach to compressible flows and in particular to the problem of shock-particle interaction [14, 28]. Here we adapt the model of Ling et al. [14] to the present problem of shock interaction with a deformable particle.

5.1 Modeling of momentum transfer

The overall hydrodynamic force is expressed as the sum of individual contributions,

$$f = f_{qs} + f_{pg} + f_{am} + f_{vu}\,, \tag{18}$$

where f_{qs}, f_{pg}, f_{am}, and f_{vu} denote the quasi-steady, pressure-gradient, added-mass, and viscous-unsteady force contributions, respectively.

The quasi-steady force f_{qs} is the force that acts on a particle due to non-zero relative velocity $(u^a - u^p)$, the expression of which is

$$f_{qs} = \frac{\overline{u^a}^s - \overline{u^p}}{\tau_v^p}\frac{C_D(\mathrm{Re}^p, \mathrm{M}^p)\mathrm{Re}^p}{24}\,, \tag{19}$$

where $\overline{u^a}^s$ is the surface-average undisturbed ambient velocity and C_D is the quasi-steady drag coefficient.

In the traditional point-particle approach, u^a will correspond to undisturbed ambient flow velocity at the particle location (or as seen by the particle). In the limit of a particle much smaller than the scale of the ambient flow, u^a can be unambiguously defined. However, in the present context of a shock wave passing over the particle, the length scale of the shock is

smaller than the particle. As a result, the undisturbed ambient flow velocity varies over the particle when the shock is located over the particle. For such spatially varying flows, in the context where compressibility is important, it has recently been rigorously derived that the appropriate representation for the ambient flow is given by an average over the surface of the particle $\overline{u^a}^s = \oint_s u^a ds$ [30].

In compressible flows, C_D is a function of particle Reynolds and Mach numbers, the expression of which is given in [28]. For dense particulate flows, C_D will depend on the particle volume fraction, see e.g., [16, 35], but the effect of finite particle volume fraction is not considered in this study. The definitions of the particle Reynolds number Re^p and Mach number M^p are

$$\mathrm{Re}^p = \frac{\overline{\rho^a}^s |\overline{u^p} - \overline{u^a}^s| d^p}{\mu^a}, \tag{20}$$

and

$$\mathrm{M}^p = \frac{|\overline{u^p} - \overline{u^a}^s|}{\overline{a^a}^s}. \tag{21}$$

The pressure-gradient force f_{pg} is the force experienced in the absence of the particle by the ambient medium that would occupy the volume of the particle. Therefore, f_{pg} depends on the stress gradient of the local undisturbed flow (the flow when the particle is absent). Though it is conventionally called pressure-gradient force, it also takes viscous stress into account. Nevertheless, in the context of shock-particle interaction, the viscous stress is negligible when compared to the pressure. As a result, f_{pg} can be expressed as

$$f_{pg} = -\frac{1}{\overline{\rho^p}} \overline{\left(\frac{\partial p^a}{\partial x}\right)}^v. \tag{22}$$

As addressed above for the quasi-steady force, the pressure gradient of the undisturbed ambient $\partial p^a/\partial x$ varies across the shock. It has been rigorously shown that in the evaluation of the pressure-gradient force, a volume average is appropriate as represented by $\overline{(\partial p^a/\partial x)}^v$ [30].

The added-mass force f_{am} is the extra force that is exerted on the particle in order to accelerate the medium surrounding the particle, when the relative acceleration between the particle and ambience is non-zero. This is the consequence of non-penetration boundary condition at the interface between the particle and the ambient medium. In compressible flows, due to finite propagation speed of acoustic waves, the added-mass force involves a history integral (see [17, 26]) and as a result the term "added mass" is not strictly appropriate. In the case of a non-deformable particle, it can be expressed as

$$f_{am} = \int_{-\infty}^{t} K_{iu}(t-\chi, \mathrm{M}^p) \left(\overline{\frac{D}{Dt}}^v \left(\frac{\overline{\rho^a u^a}^v}{\overline{\rho^p}} \right) - \frac{d}{dt} \left(\frac{\overline{\rho^a}^v \overline{u^p}}{\overline{\rho^p}} \right) \right)_{t=\chi} d\chi, \tag{23}$$

where K_{iu} is the inviscid unsteady kernel. As shown by [17] and [26] in the limit of zero Mach number, the kernel takes a simple form $K_{iu}(\xi) = \exp(-\xi)\cos(\xi)$. At finite M^p, K_{iu} cannot be derived analytically, but numerical solutions were presented by [26]. In the present context of a strong shock interacting with a deformable particle, additional complexities arise. Discussions on modeling added-mass force for a deformable particle will be presented in the following section.

At last, the viscous-unsteady force f_{vu}, which is often called the Basset history force, is the viscous force exerted on a particle due to temporal development of the boundary layer when the relative acceleration between the particle and ambient medium is non-zero. The expression of viscous-unsteady force is given as

$$f_{vu} = \frac{1}{\overline{\rho^a}^s \tau_v^p} \int_{-\infty}^{t} K_{vu}(t-\chi, \mathrm{Re}^p, \mathrm{M}^p) \left(\overline{\frac{D}{Dt}}^s \overline{(\rho^a u^a)}^s - \frac{d}{dt} \overline{(\rho^a u^p)}^s \right)_{t=\chi} d\chi, \tag{24}$$

where the viscous-unsteady kernel is denoted by K_{vu}. In incompressible flows, models of K_{vu} for finite Reynolds numbers is given by [19] and [13]. Expressions of K_{vu} in compressible flows in the limit of Re^p, $\mathrm{M}^p \to 0$ can be found in [29]. Corresponding kernel for compressible flows for finite Re^p and M^p are not fully understood. Nevertheless, the primary focus here is the initial inviscid-phase and thus viscous steady force is of secondary importance.

A detailed discussion about using surface or volume averaged quantities in a non-uniform flow can be found in [30] and [14]. The averaged substantial derivatives $\overline{D/Dt}^s$ and $\overline{D/Dt}^v$ are defined as

$$\overline{\frac{D}{Dt}}^s = \frac{\partial}{\partial t} + \overline{u^a}^s \frac{\partial}{\partial x}\,, \tag{25}$$

$$\overline{\frac{D}{Dt}}^v = \frac{\partial}{\partial t} + \overline{u^a}^v \frac{\partial}{\partial x}\,. \tag{26}$$

5.2 Modeling of added-mass force

When a strong shock wave interacts with a deformable particle, the inviscid instead kernel K_{iu} will not only depend on M^p, but also on the shape of the deformable particle. Since the detailed depedance of the kernel is not known for shapes other than spheres and cylinders, here we pursue a simpler integrated approach. In this appoach, Eq. (23) is simplified to

$$f_{am} = \overline{\frac{D}{Dt}}^v \left(\frac{C_M \overline{\rho^a u^a}^v}{\overline{\rho^p}} \right) - \frac{d}{dt} \left(\frac{C_M \overline{\rho^a}^v \overline{u^p}}{\overline{\rho^p}} \right)\,, \tag{27}$$

where the evaluation of the history integral is altogether avoided. Here C_M is the effective added-mass coefficient, which in the present problem can be taken to depend on both the instantaneous particle Mach number (Eq. (21) and the shape of the particle. Note that $C_M = 0.5$ for a spherical particle in incompressible flow. As shown in [26], the effective added-mass coefficient increases with M^p. Furthermore, as seen in the DNS simulation results, Figs. 5 and 6, the spherical particle can be seen to compress and take an oblate spheroid shape. The added-mass coefficient of oblate objects is larger than that of a sphere. As a result, the effective added-mass coefficient substantially increases during shock-particle interaction and therefore it cannot be taken to be a constant.

Replacing the history integral Eq. (23) by Eq. (27) is a significant (but unavoidable) approximation. The kernel K_{iu} has been established to exponentially decay on acoustic time scale. If the time rate of change of relative momentum $\overline{\frac{D}{Dt}}^v \left(\overline{\rho^a u^a}^v / \overline{\rho^p}\right) - \frac{d}{dt}\left(\overline{\rho^a}^v \overline{u^p} / \overline{\rho^p}\right)$ were to be slow on the acoustic time scale, then Eq. (27) will be a good approximation to Eq. (23). However, unfortunately, in the context of shock-particle interaction, the time rate of change of relative momentum occurs on the acoustic time scale and thus Eq. (27) is only an approximation. Even though the detailed time evolution of the added-mass force on the acoustic time scale cannot be reproduced with the approximation Eq. (27), with an appropriate device of C_M we will recover the overall effect of the inviscid unsteady force.

To account for the effect of particle deformation and compressibility on added-mass coefficient, the effective added-mass coefficient,C_M, can be written as:

$$C_M(t) = C_{M,0}\xi(t)\eta(\mathrm{M}^p)\,, \tag{28}$$

where $C_{M,0}$ is the initial added-mass coefficient of the particle, and ξ and η are the correction functions that take into account the effects of particle deformation and compressibility of the ambient medium. It has been shown in Fig. 6, the particle deformation mainly occurs as the shock wave passes through. After that, the change of particle shape becomes small and has less influence on the added-mass force. Therefore, a simple expression for ξ is proposed as

$$\xi(t) = 1 + \left(\frac{C_{M,F}}{C_{M,0}} - 1 \right)(1 - e^{-t/\tau_s})\,, \tag{29}$$

where $C_{M,F}$ is the final added-mass coefficient of the particle. As the shape of the particle is initially spherical, $C_{M,0} = 0.5$. The value of $C_{M,F}$ depends on the final shape, which in turn depends on the particle material and the shock strength. Therefore, $C_{M,F}$ may vary from case to case and can be considered as an input to the model. It is shown in Fig. 5 that the final shape of the aluminum particle is similar to an oblate spheroid. The added-mass coefficient for a spheroid is a function of the ratio between equatorial radius r_{eq} and conjugate radius r_{co} [23]. In the limit of $r_{co}/r_{eq} = 0$, $C_M = 1$. It has also been observed that a spherical particle can deform and end up with a torus shape [22]. For a torus, C_M is about 1 [21]. In general, $C_{M,F} = 1$ is a reasonable approximation if the final shape of the particle is not known *a priori*.

In addition, when the shock wave passes over the particle, M^p is finite and contribute to further increase in the value of C_M. It is shown in [26] that, for a spherical particle, C_M for $\mathrm{M}^p = 0.6$ is about twice of that for $\mathrm{M}^p = 0$. The expression of η are given by Parmar et al.[26]

$$\eta(\mathrm{M}^p) = 1 + 1.8(\mathrm{M}^p)^2 + 7.6(\mathrm{M}^p)^4 \,. \tag{30}$$

When particle Mach number approaches zero and particle is rigid, ξ and η both reduce to unity and we recover $C_M = C_{M,0} = 0.5$. When particle deformation is negligible but M^p is finite, Eq. (28) reduces to the numerical correlation of effective finite-Mach-number added-mass coefficient for a sphere [26]. Note that Parmar et al.[26] only considered the particle Mach number up to the critical Mach number, therefore, Eq. (30) is valid for $\mathrm{M}^p \leq \mathrm{M}^p_{cr}$. It has been verified that this condition is satisfied for all cases considered here.

5.3 Modeling of energy transfer

Similarly to the force analysis, the overall heating exerted on a particle can be expressed as the sum of different contributions

$$q = q_{qs} + q_{uu} + q_{du} \,, \tag{31}$$

where q_{qs}, q_{uu}, and q_{du} denote the quasi-steady, undisturbed-unsteady, and diffusive-unsteady heating contributions, respectively.

The quasi-steady heating contribution q_{qs} is the thermal analog of quasi-steady force, which is the heat transfered from the ambient medium to the particle due to non-zero relative temperature $(T^a - T^p)$. This can be the expressed as

$$q_{qs} = \frac{\overline{T^a}^s - \overline{T^p}}{\tau^p_\theta} \frac{\mathrm{Nu}(\mathrm{Re}^p, \mathrm{Pr}^a, \mathrm{M}^p)}{2} \,, \tag{32}$$

where Nu is the Nusselt number, which is a function of the particle Reynolds and Mach numbers as well as the Prandtl number of the ambient medium. An empirical correlation of Nu in compressible flows is given in [8].

The undisturbed-unsteady heating contribution, q_{uu}, accounts for the energy transfer due to the unsteadiness of the undisturbed ambient flow field, which includes heat conduction and work done by the surface stresses on the volume of ambient medium replaced by the particle [15]. In the present problem of SIDP, since the particle deforms during the interaction with the shock wave, additional challenges arise in modeling of q_{uu}. The details of the model for q_{uu} will be presented in the following section.

The diffusive-unsteady heating contribution, q_{du}, is the thermal analog of viscous-unsteady force, which accounts for the unsteady thermal diffusion due to the temporal development of the thermal boundary layer around the particle and depends on the past history of relative thermal acceleration. The expression of q_{du} is

$$\begin{aligned} q_{du} = & \frac{1}{2\rho^a \tau^p_\theta} \int_{-\infty}^{t} K_{du}(t-\chi, \mathrm{Re}^p, \mathrm{Pr}^a, \mathrm{M}^p) \\ & \left(\overline{\frac{D}{Dt}}^s \overline{(\rho^a T^a)}^s - \frac{d}{dt} \overline{(\rho^a T^p)}^s \right) d\chi \,, \end{aligned} \tag{33}$$

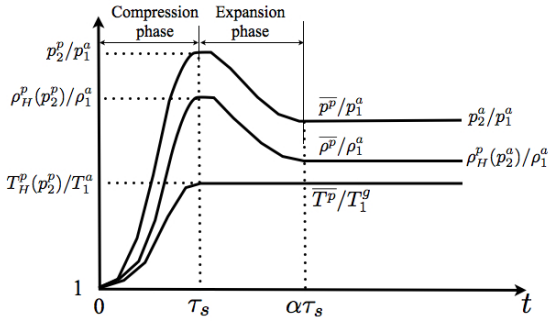

Fig. 11 Schematic representation for evolutions of pressure, density, and temperature according to the present model.

where K_{du} is the diffusive-unsteady heating kernel. In the limit of zero particle Reynolds and Mach numbers, K_{du} is identical to K_{vu}, see [20]. Extensions for finite particle Reynolds number were presented by [7] and [2]. To our knowledge, there is no previous work in the literature on the kernel for compressible flows. As suggested in [14], the kernel presented in [7] can be used as an approximation. Nevertheless, during the early inviscid-phase of SIDP, the contribution of the diffusive-unsteady heating is not significant.

5.4 Modeling of compression heating

In the inviscid phase of SIDP, the compression work done by pressure is much larger than that by the shear stress and the heat transfer between the particle and ambient medium. As a result, the undisturbed-unsteady heating contribution reduces to compression heating which can be expressed as

$$q_{uu} = -\frac{1}{\rho^p C^p} p^p \overline{\frac{\partial u_i^p}{\partial x_i}}^v \quad . \tag{34}$$

However, in the interaction with an intense shock wave, the particle deforms significantly. The velocity and thermal properties inside the particle are non-uniform and vary in time in a complex manner. Therefore, Eq. (34) is still too complicated for calculating the evolution of the mean particle temperature. Hence, additional modeling is required.

Instead of computing the compression work, we can take advantage of the knowledge we obtained from the DNS results to model the evolution of average particle temperature directly. In Fig. 10(b), it can be seen that the temperature on the Hugoniot curve corresponding to p_2^p, denoted as $T_H^p(p_2^p)$, can be used as approximation for the final average particle temperature in the inviscid phase. Here, p_2^p is the pressure behind the transmitted-shock in the 1D analog of shock-particle interaction, see Fig. 9, which can be fully determined by shock strength and the material properties of the particle and ambient medium. For Cases 1 and 2 considered in the present study, we have computed $p_2^p = 4.14$ and 20.9 GPa, respectively. Tracer 1 is located at the leading point of the spherical particle. When the incident shock reaches tracer 1, the spherical geometry has little effect on its response to the shock wave. As a result, the post-transmitted-shock pressure of tracer 1 is observed to be very close to p_2^p. Nevertheless, tracer 1 also experiences the effect of multiple expansions and compressions that do not follow the 1D model of Fig. 9.

Therefore, we propose to model the evolution of thermodynamic properties in the inviscid phase as follows. The inviscid-phase of SIDP is considered to consist of two stages in the model. The first stage is the *compression stage*, which is used to model the process when the transmitted shock is passing through the particle. The transmitted shock curvature is ignored and the transmitted shock is assumed to pass through with a constant speed that is approximated by the incident shock speed. The mass average particle pressure $\overline{p^p}_{\text{inv}}$, density $\overline{\rho^p}_{\text{inv}}$, and temperature $\overline{T^p}_{\text{inv}}$ increases from (p_1^a, ρ_1^p, T_1^a) to (p_2^p, $\rho_H^p(p_2^p)$, $T_H^p(p_2^p)$) in τ_s, see Fig. 11.

The second stage is the *expansion stage*, which actually models the subsequent expansion and compression processes inside the particle after the shock passage. We consider the particle to reach the asymptotic final state at the end of the expansion stage. From Fig. 8, it can be seen that the expansion stage for Case 1 ends at about $4\tau_s$. When shock strength or material property change, the normalized time duration of the expansion stage will vary. As shown in Fig. 8(b), the detailed evolution of the expansion state is non-monotonic. However, these oscillations in the particle pressure occur on the scale of τ_s and thus are of secondary importance if the time scale of interest is much larger than τ_s. In the present model, $\overline{p^p_{\text{inv}}}$ and $\overline{\rho^p_{\text{inv}}}$ are taken decrease monotonically from $(p^p_2, \rho^p_H(p^p_2))$ to $(p^a_2, \rho^p_H(p^a_2))$. From the DNS results, Figs. 8(b) and 10(b), the expansion stage is nearly isothermal. Therefore, $\overline{T^p_{\text{inv}}}$ remains close to $T^p_H(p^p_2)$. The asymptotic final states in the inviscid-phase of SIDP represented by the present model are also indicated in Figs. 8 and 10. In Figs. 8(b) and 10(b), it can be seen that the asymptotic final temperature given by the model is lower than that computed by DNS. This discrepancy is related to the approximation in the present model, i.e., the details of the subsequent expansion and compression processes inside the particle after the shock passage and their effects on the particle temperature evolution are ignored. Though the subsequent expansion and compression waves inside the particle decay fast, their overall influences on the particle temperature are not small. Therefore, the present model captures only the leading order effect of shock compression heating on the particle. Due to the spherical geometry, the expansion and compression processes inside the particle are quite complex, see Fig. 6. To improve the capability of the model on capturing the final temperature in the inviscid-phase of SIDP, a more sophisticated model that takes into account these wave interactions is needed.

In summary, the evolutions for mass average particle thermal properties in the inviscid-phase of SIDP can be expressed as

$$\overline{p^p_{\text{inv}}} = \begin{cases} \phi p^p_2 + (1-\phi)p^a_1, & 0 < \tilde{t} < 1 \\ \psi p^a_2 + (1-\psi)p^p_2, & 1 < \tilde{t} < \alpha \\ p^a_2, & \tilde{t} > \alpha\,, \end{cases} \tag{35}$$

$$\frac{1}{\overline{\rho^p_{\text{inv}}}} = \begin{cases} \dfrac{\phi}{\rho^p_H(p^p_2)} + \dfrac{1-\phi}{\rho^p_1}, & 0 < \tilde{t} < 1 \\ \dfrac{\psi}{\rho^p_H(p^a_2)} + \dfrac{1-\psi}{\rho^p_2}, & 1 < \tilde{t} < \alpha \\ \rho^p_H(p^a_2), & \tilde{t} > \alpha\,, \end{cases} \tag{36}$$

$$\overline{T^p_{\text{inv}}} = \begin{cases} \phi T^p_H(p^p_2) + (1-\phi)T^a_1, & 0 < \tilde{t} < 1 \\ T^p_H(p^p_2), & \tilde{t} > 1\,, \end{cases} \tag{37}$$

where $\tilde{t} = t/\tau_s$. The expressions for weight functions ϕ and ψ are given as

$$\phi(\tilde{t}) = 3\tilde{t}^2 - 2\tilde{t}^3\,, \tag{38}$$

$$\psi(\tilde{t}) = 3\left(\frac{\tilde{t}-1}{\alpha-1}\right)^2 - 2\left(\frac{\tilde{t}-1}{\alpha-1}\right)^3\,. \tag{39}$$

The weight functions ϕ and ψ increase smoothly from 0 to 1 when $\tilde{t}$ increases from 0 to 1 and from 1 to α, respectively. The form of the weight function is chosen here following the work by Parmar et al.[27]. The time duration of inviscid-phase of SIDP normalized by τ_s is indicated by α, which changes with the shock strength and the material properties of the particle and ambient medium. For simplicity, α is taken to be 2 for the results shown in section 6.

In the above model, the post-incident-shock pressure in the ambient medium, p^a_2, and the post-transmitted-shock pressure when a shock wave interacts with a 1D particle, p^p_2, are inputs of the model. With the Rankine-Hugoniot relation, T^a_2 and ρ^a_2 can be computed from p^a_2, and $T^p_H(p^p_2)$ and $\rho^p_H(p^p_2)$ can be computed from p^p_2.

6 Point-particle results and validation

The models presented in section 5 is used to compute the mass average particle velocity and

temperature for the same cases that were studied by DNS in section 4 (see Table 2). The results computed using the point-particle models are compared to those achieved by DNS for validation. Since the particle and the ambient medium are considered as inviscid in DNS, only the inviscid forces (Eqs. (22) and (27)) and the compression heating contribution (Eqs. (35)–(37)) in the models are active. To highlight the importance of the inviscid unsteady force and compression heating, the results computed by the standard drag [5] and heat-transfer correlations [42] are also shown. We also apply the models to compute a case of particle interaction with a CJ detonation wave and the results will be compare against those obtained using DNS by Ripley [33].

6.1 Particle interaction with a non-reacting shock wave

The temporal evolution of the mass average velocity and temperature of an aluminum particle subjected to a nitromethane shock wave for Cases 1 and 2 are shown in Figs. 12 and 13, resepetively. From Fig. 12, it can be seen that $\overline{u^p}$ rises rapidly when the transmitted shock passes through the particle. The mass average particle velocity reaches its maximum value at around $t = \tau_s$. This rapid increase of $\overline{u^p}$ when the shock passes through is reasonably captured by the present model. Up to the time plotted here, the maximum values of $\overline{u^p}$ computed by the present model are about 50% and 58% of u_2^a for Cases 1 and 2, respectively; while those computed by DNS are about 58% and 65% of u_2^a, respectively. Comparing Cases 1 and 2, the maximum $\overline{u^p}$ increases with shock strength. This trend is captured by the model as well. If the standard drag law is used, it can be seen that the rapid acceleration of the particle during the passage of the shock wave is completely missed. This highlights the critical importance of the inviscid unsteady force in the point-particle calculation of the particle motion in SIDP problems.

For $t > \tau_s$, $\overline{u^p}$ continues to increase more gradually until reaching an intermediate asymptotic value. As we consider both the particle and ambient medium to be inviscid in the DNS, $\overline{u^p}$ will reach an asymptotic value that is different from the ambient medium. Particle deformation contributes to the increase in the added-mass force exerted on the particle. If particle deformation is ignored in computing the added-mass force, i.e., $C_M = 0.5$, the particle velocity increase will be underestimated as shown in Fig. 12(b). With increasing shock strength, the particle deforms more severely and the contribution of particle deformation on increasing the particle velocity is more profound for Case 2 than Case 1. For Case 1, due to the relatively low shock strength and small particle deformation, the results of $C_M = 0.5$ are very similar to those of the present model. Furthermore, when the shock is stronger, it takes longer time for the particle to settle to its final shape. The present model recovers the overall trend of $\overline{u^p}$ after the shock passage quite well, but in general, the present model underestimate $\overline{u^p}$ by about 10-15%. The discrepancy is partially related to the details of particle deformation that are neglected in the calculation of the particle force. For Case 2, the DNS results by Ripley [33] is also shown here, which agrees with the present DNS and model results reasonably well.

Similarly, the mass average particle temperature increases rapidly when the shock wave passes by, see Fig. 13. It is seen that $\overline{T^p} - T_1^a$ can reach about 12% and 17% of $T_2^a - T_1^a$ for Cases 1 and 2, respectively. The evolution of $\overline{T^p}$ obtained through DNS is in general more complex. The approach to the asymptotic state for $\overline{T^p}$ exhibits oscillations. These oscillations are due to the repeated reflection of the compression and expansion waves inside the particle. Due to the lateral expansion described in section 4, $\overline{T^p}$ reaches a local maxima before $t = \tau_s$. Neverthe-

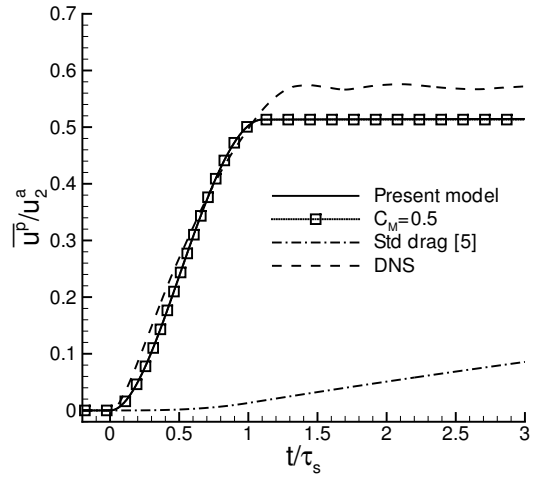

(a) Case 1

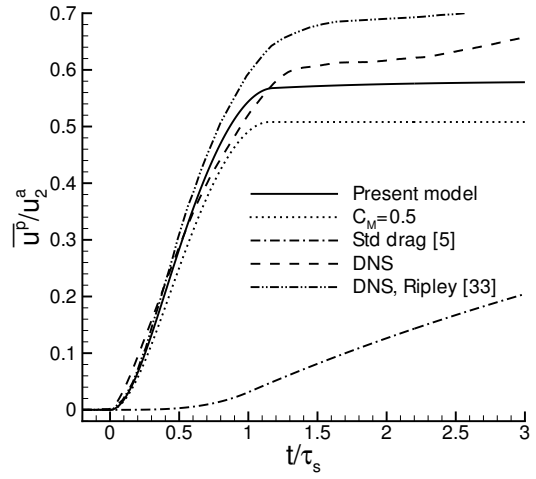

(b) Case 2

Fig. 12 Time evolutions of average particle velocity for (a) Case 1 and (b) Case 2.

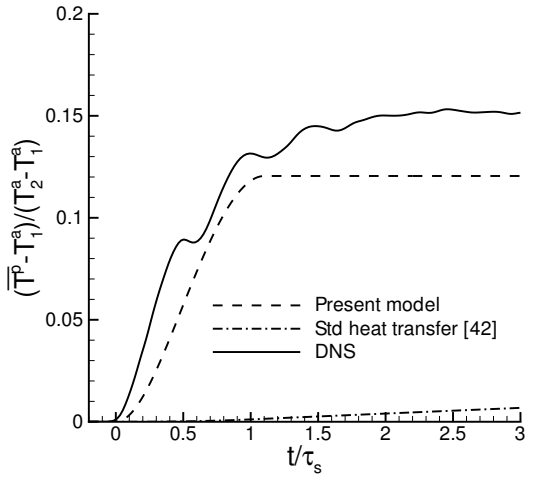

(a) Case 1

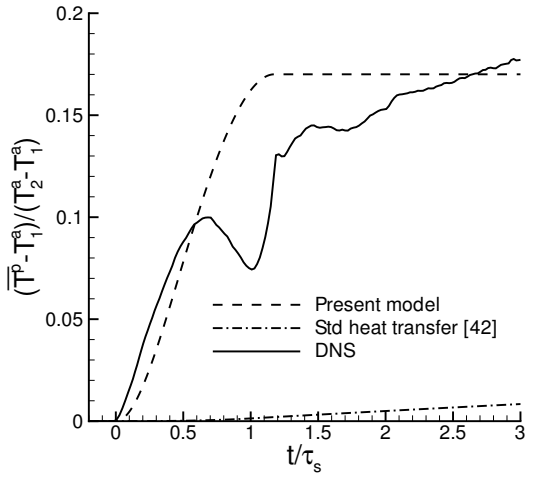

(b) Case 2

Fig. 13 Time evolutions of average particle temperature for (a) Case 1 and (b) Case 2.

less, the present model captures the rapid temperature rise which is missed by the standard heat-transfer correlation.

In the DNS results, $\overline{T^p}$ continues to increase after the shock passage until an asymptotic state is reached. It can be observed in Fig. 13(a) that, $\overline{T^p}$ for case 1 reaches its final value at about $t = 2.5\tau_s$. When the shock strength increases, the compression heating effect becomes stronger and $\overline{T^p}$ increases accordingly. Similar to the particle velocity evolution, the particle temperature takes longer time to reach the asymptotic state for case 2 than case 1. Since the model ignores the contributions of the subsequent expansion

and compression processes after the shock passage, it does not recover the oscillations in the evolution of $\overline{T^p}$ and also the slow increase in $\overline{T^p}$ after the shock passage. Due to this simplification, the model underestimates the final asymptotic average particle temperature compared to the DNS results. In order to obtain a better estimate on the temperature evolution, a more sophisticated model that takes into account the subsequent wave reflection and refractions at the particle interface is needed, which is relegated to future work.

6.2 Particle interaction with CJ detonation

We also apply the models to the problem of particle interaction with a detonation wave for the case considered by Ripley [33]. As discussed in [33], when the particle diameter is much smaller or larger than the reaction zone, the structure of the reaction zone behind the detonation wave has little influence on interaction with a particle. When particle is much larger than the reaction zone, the reaction zone combined with the shock wave can be viewed as a discontinuity, i.e., as a CJ detonation wave [3, 12]. Ripley [33] has carried out a direct numerical simulation for the problem of a spherical aluminum particle interacting with a CJ detonation wave in nitromethane. Here, we study the same problem using the present point-particle models. In [33], the particle and the ambient medium are assumed to be inviscid, therefore, the inviscid forces and the compression heating are used to compute the mass average particle velocity and temperature.

Following the work of Ripley [33], the detonation wave propagation distance is taken to be much larger than the particle diameter. As a result, the effect the expansion wave behind the detonation wave (the so-called Taylor wave [39]) on the particle is ignored. Then the properties of the gaseous products behind the CJ detonation wave can be considered as constant. The CJ conditions for the problem studied here can be found in [33], which are listed in Table 3 as well.

u_{si} [m/s]	u^a_{CJ} [m/s]	p^a_{CJ} [GPa]	ρ^a_{CJ} [Kg/m^3]	T^a_{CJ} [K]
6690	1756	13.3	1530	3591

Table 3 CJ conditions for the case of particle interaction with a CJ detonation wave [33].

The evolutions of average particle velocity and temperature for an aluminum particle interacting with a CJ detonation in nitromethane are shown in Fig. 14. The subscript "CJ" is used to denote post-CJ-detonation quantities. It can be seen that the evolutions of $\overline{u^p}$ and $\overline{T^p}$ for detonation-particle interaction is quite similar to the non-reacting shock cases. Both $\overline{u^p}$ and $\overline{T^p}$ increase rapidly when the detonation wave passes the particle. The model captures the rapid rises in $\overline{u^p}$ and $\overline{T^p}$ pretty well. For the evolution of $\overline{u^p}$ during the interval $0 < t < \tau_s$, the agreement between the model and the DNS results is excellent. It can be also observed that, when the standard quasi-steady drag law [5] (which ignores the inviscid unsteady force) is used, the rapid particle acceleration is missed. After the passage of the detonation wave, $\overline{u^p}$ continues to grow due to particle deformation as discussed before. By including the detailed history of particle deformation in the model, the continual increase of $\overline{u^p}$ could be better captured. The deviation between the model and DNS results increases with time. Nevertheless, the deviation in $\overline{u^p}$ is less than 15% for $t < 3\tau_s$. Beyond the simplifications involved in the model, the numerical approximation and errors in DNS may also contribute to the discrepancy.

Since chemical energy of nitromethane is released in the detonation wave, the post-detonation temperature of nitromethane detonation products is much larger than that behind a non-reacting shock. As a result, $(T^a_{CJ} - T^a_1)$ is much

larger than $(T_2^a - T_1^a)$ in the non-reacting shock cases. As in the DNS, we consider the aluminum particle to remain inert, so the particle temperature increases only due to detonation-compression heating. Therefore, $(\overline{T^p} - T_1^p)/(T_{CJ}^a - T_1^a)$ here in the detonation case is an order of magnitude smaller than the non-reacting shock cases. The overall trend of the mass average particle temperature computed by the present model matches the DNS results reasonably well. The rapid thermal acceleration of the particle is missed by the standard heat-transfer law [42]. Again, due to subsequent compression and expansion waves that repeatedly get reflected within the particle after the passage of the detonation wave, the particle temperature approaches the asymptotic value in an oscillatory manner. This effect is not recovered by the present simple model, as the effects of the subsequent wave interactions are not taken into account. Nevertheless, the model predicts the final value of $\overline{T^p}$. In a macro-scale simulation, the oscillations in particle thermal evolution occur over acoustic time scale and thus are in general of secondary importance. If these oscillations in particle thermal evolutions are of concern, then a more sophisticated model needs to be developed to take into account the subsequent compression and expansion waves within the particle.

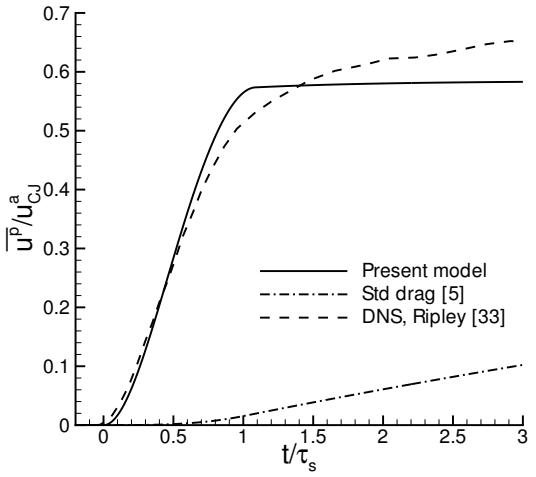

(a) Velocity

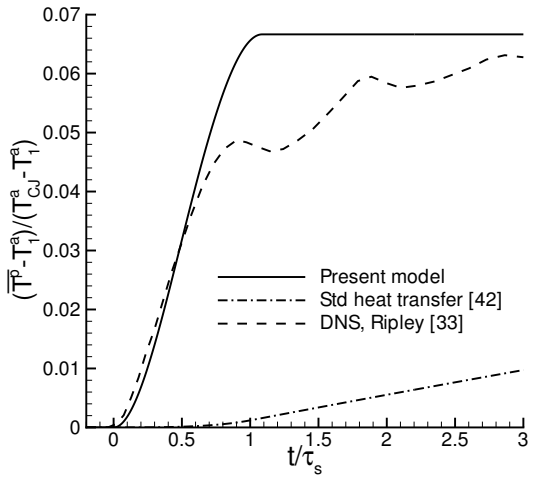

(b) Temperature

Fig. 14 Time evolutions of average particle velocity and temperature for an aluminum particle interacting with a nitromethane CJ-detonation.

7 Conclusions

In this paper, we investigate the problem of shock interaction with a deformable particle (SIDP) through scaling analysis and direct numerical simulations. Based on previous work on shock interaction with a rigid particle [14], we proposed point-particle models for the momentum and thermal evolution of the deformable particle in the context of SIDP. A qualitative analysis of SIDP identifies the shock impedance ratio and the shock speed ratio as the two key parameters that control the nature of particle deformation and the shock defraction pattern around the particle. Simple estimates for the shock impedance ratio and shock speed ratio are obtained for the limit of a very strong shock. When both the spherical particle and the ambient medium are condensed matter, the generated shock refraction pattern is expected to be different from that in a gas-gas system. Time

scale analysis shows that the overall interaction process can be split into inviscid and viscous phases according to the dominant mechanism. In the inviscid phase, particle velocity primarily evolves due to the inviscid unsteady interaction with the primary shock wave and the subsequent internally reflected wave interactions. The corresponding thermal evolution of the particle during the inviscid phase is controlled by compression heating. The code ALE3D is used to conduct direct numerical simulations of the inviscid phase of the interaction for the particular case of a spherical aluminum particle subjected to an intense shock wave in nitromethane under non-reacting condition. Two different shock strengths are considered and it is found that the particle can gain significant velocity and temperature through the initial inviscid interaction with the shock wave. The particle is observed to deform substantially and the effect of particle deformation must be accounted in the models of interphase coupling. A simple physics-based model is proposed to capture the essential physics of interphase coupling in SIDP based on the previous work of Ling et al.[14]. The present model takes into account the effect of particle deformation on the added-mass force and the effect of unsteady compression on heating the particle. The model prediction is compared to the DNS results, and reasonable agreement is observed. In particular, the present models offer significant improvements over the standard force and heat transfer models [5, 42], through the inclusion of the unsteady mechanisms and deformation effects.

Acknowledgment

The authors would like to acknowledge support from AFOSR under grant FA 9550-10-1-0309. The direct numerical simulations in this paper was performed under the auspices of the U.S. Department of Energy by Lawrence Livermore National Laboratory under Contract DE-AC52-07NA27344. This work was partially funded by the Joint DOD/DOE Munitions Technology Development Program and we acknowledge the DOE NNSA/ASC program for its support of ALE3D.

References

1. S. Balachandar and J. K. Eaton. Turbulent dispersed multiphase flow. *Annu. Rev. Fluid Mech.*, 42:111–133, 2010.
2. S. Balachandar and M. Y. Ha. Unsteady heat transfer from a sphere in a uniform cross-flow. *Phys. Fluids*, 13:3714–3728, 2001.
3. D. L. Chapman. On the rate of explosion in gases. *Phil. Mag.*, 47:90–104, 1889.
4. A. Chauvin, G. Jourdan, E. Daniel, L. Houas, and R. Tosello. Experimental investigation of the propagation of a planar shock wave through a two-phase gas-liquid medium. *Phys. Fluids*, 23:113301, 2011.
5. R. Clift and W. H. Gauvin. The motion of particles in turbulent gas streams. *Proc. Chemeca*, 1:14–28, 1970.
6. C. T. Crowe. Numerical-models for dilute gas-particle flows - review. *J. Fluid Eng.*, 104:297–303, 1982.
7. Z. G. Feng and E. E. Michaelides. Unsteady heat transfer from a sphere at small peclet numbers. *J. Fluid Eng.-T. ASME*, 118:96–102, 1996.
8. T. W. Fox, C. W. Rackett, and J. A. Nicholls. Shock wave ignition of magnesium powders. In *Proc. 11th Int. Symp. Shock Tubes and Waves*, pages 262–268, Seattle, WA, 1978. University of Washington Press.
9. D. L. Frost, C. Ornthanalai, Z. Zarei, V. Tanguay, and F. Zhang. Particle momentum effects from the detonation of heterogeneous explosives. *J. Appl. Phys.*, 101: 113529, 2007.
10. D. L. Frost, S. Goroshin, and F. Zhang. Jet formation during explosive particle disper-

sal. In *International symposium on military aspects of blast and shock*, 2010.
11. L. F. Henderson. On the refraction of shock waves. *J. Fluid Mech.*, 198:365–386, 1989.
12. E. Jouguet. Sur l'onde explosive. *C. R. Acad. Sci. Paris*, 140:1211, 1904.
13. I. Kim, S. Elghobashi, and W. A. Sirignano. On the equation for spherical-particle motion: effect of Reynolds and acceleration numbers. *J. Fluid Mech.*, 367:221–253, 1998.
14. Y. Ling, A. Haselbacher, and S. Balachandar. Importance of unsteady contributions to force and heating for particles in compressible flows. Part 1: Modeling and analysis for shock-particle interaction. *Int. J. Multiphase Flow*, 37:1026–1044, 2011.
15. Y. Ling, A. Haselbacher, and S. Balachandar. Importance of unsteady contributions to force and heating for particles in compressible flows. Part 2: Application to particle dispersal by blast wave. *Int. J. Multiphase Flow*, 37:1013–1025, 2011.
16. Y. Ling, J. L. Wagner, S. J. Beresh, S. P. Kearney, and S. Balachandar. Interaction of a shock wave with a dense particle field: Modeling and experimental validation. Under review, 2012.
17. A. L. Longhorn. The unsteady, subsonic motion of a sphere in a compressible inviscid fluid. *Quart. J. Mech. Appl. Math.*, 5: 64–81, 1952.
18. M.R. Maxey and J.J. Riley. Equation of motion for a small rigid sphere in a nonuniform flow. *Phys. Fluids*, 26:883–889, 1983.
19. R. Mei and R.J. Adrian. Flow past a sphere with an oscillation in the free-stream velocity and unsteady drag at finite Reynolds number. *J. Fluid Mech.*, 237:323–341, 1992.
20. E.E. Michaelides and Z. Feng. Heat transfer from a rigid sphere in a nonuniform flow and temperature field. *Int. J. Heat Mass Transfer*, 37:2069–2076, 1994.
21. T. Miloh, G. Waisman, and D. Weihs. The added-mass coefficients of a torus. *J. Eng. Math.*, 12(1):1–13, 1978.
22. F. M. Najjar, W. M. Howard, L. E. Fried, M. R. Manaa, A. Nichols III, and G. Levesque. Computational study of 3-d hot-spot initiation in shocked insensitive high-explosive. In M. Elert, W. Buttler, J. Borg, J. Jordan, and T. Vogler, editors, *Proceedings of the Conference of the American Physical Society Topical Group on Shock Compression of Condensed Matter*, pages 255–258, 2011.
23. J. N. Newman. *Marine Hydrodynamics*. The MIT Press, 1977.
24. A. Nichols III. *User's manual for ALE3D, an Arbitrary Lagrange/Eulerian 2D and 3D Code System*. Lawrence Livermore National Laboratory, llnl-sm-404490 rev. 1 edition, 2009.
25. J. H. J. Niederhaus, J. A. Greenough, J. G. Oakley, D. Ranjan, M. H. Anderson, and R. Bonazza. A computational parameter study for the three-dimensional shock-bubble interaction. *J. Fluid Mech.*, 594:85–124, 2008.
26. M. Parmar, A. Haselbacher, and S. Balachandar. On the unsteady inviscid force on cylinders and spheres in subcritical compressible flow. *Phil. Trans. R. Soc. A*, 366: 2161–2175, 2008.
27. M. Parmar, A. Haselbacher, and S. Balachandar. Modeling of the unsteady force for shock–particle interaction. *Shock Waves*, 19:317–329, 2009.
28. M. Parmar, A. Haselbacher, and S. Balachandar. Improved drag correlation for spheres and application to shock-tube experiments. *AIAA J.*, 48:1273–1276, 2010.
29. M. Parmar, A. Haselbacher, and S. Balachandar. Generalized Basset-Boussinesq-Oseen equation for unsteady forces on a sphere in a compressible flow. *Phys. Rev. Lett.*, 106:084501, 2011.

30. M. Parmar, A. Haselbacher, and S. Balachandar. Equation of motion for a sphere in equation of motion for a sphere in non-uniform compressible flows. *J. Fluid Mech.*, 2012.
31. J. J. Quirk and S. Karni. On the dynamics of a shock-bubble interaction. *J. Fluid Mech.*, 318:129–163, 1996.
32. D. Ranjan, J. Oakley, and R. Bonazza. Shock-bubble interactions. *Annu. Rev. Fluid Mech.*, 43:117–140, 2011.
33. R. C. Ripley. *Acceleration and heating of metal particles in condensed matter detonation.* PhD thesis, University of Waterloo, 2010.
34. R.C. Ripley, F. Zhang, and F.-S. Lien. Shock interaction of metal particles in condensed explosive detonation. *AIP Conf. Proc.*, 845:499–502, 2006.
35. A. S. Sangani, D. Z. Zhang, and A. Prosperetti. The added mass, basset, and viscous drag coefficients in nondilute bubbly liquids undergoing small-amplitude oscillatory motion. *Phys. Fluids A*, 3:2955, 1991.
36. B. W. Skews, M. S. Bredin, and M. Efune. Drag measurements in unsteady compressible flow. part 2: Shock wave loading of spheres and cones. *R&D J. South Afr. Inst. Mech. Eng.*, 23:13–19, 2007.
37. M. Sun, T. Saito, K. Takayama, and H. Tanno. Unsteady drag on a sphere by shock wave loading. *Shock Waves*, 14:3–9, 2005.
38. K. Takayama and T. Saito. Shock wave/geophysical and medical applications. *Annu. Rev. Fluid Mech.*, 36:347–379, 2004.
39. G. I. Taylor. The dynamics of the combustion products behind plane and spherical detonation fronts in explosives. *Proc. R. Soc. Lond. A Mat.*, 200:235–247, January 1950.
40. J. von Neumann and R. D. Richtmyer. A method for the numerical calculation of hydrodynamic shocks. *J. Appl. Phys.*, 21(232-237), 1950.
41. J. M. Walsh and R. H. Christian. Equation of state of metals from shock wave measurements. *Phys. Rev.*, 97:1544–1556, 1955.
42. S. Whitaker. Forced convection heat transfer correlations for flow in pipes, past flat plates, single spheres, and for flow in packed beds and tube bundles. *AIChE J.*, 18:361–371, 1972.
43. Z. Zarei and D. L. Frost. Simplified modeling of blast waves from metalized heterogeneous explosives simplified modeling of blast waves from metalized heterogeneous explosives. *Shock Waves*, 21:425–438, 2011.
44. F. Zhang, D. L. Frost, P. A. Thibault, and S. B. Murray. Explosive dispersal of solid particles. *Shock Waves*, 10:431–443, 2001.
45. F. Zhang, P. A. Thibault, and R. Link. Shock interaction with solid particles in condensed matter and related momentum transfer. *Proc. R. Soc. Lond. A Mat.*, 459: 705–726, 2003.
46. F. Zhang, K. Gerrard, and R. C. Ripley. Reaction mechanism of Aluminum-particle-air detonation. *J. Propul. Power*, 25:845–858, 2009.